A Comprehensive Study on Magnetoelectric Transducers for Wireless Power Transfer Using Low-Frequency Magnetic Fields

Sujay Hosur[®], *Student Member, IEEE*, Rammohan Sriramdas, Sumanta Kumar Karan, Na Liu, Shashank Priya[®], and Mehdi Kiani[®], *Senior Member, IEEE*

Abstract—Magnetoelectric (ME) transducers, comprising of layered magnetostrictive and piezoelectric materials, are more efficient than inductive coils in converting low-frequency magnetic fields into electric fields, particularly in applications that require miniaturized devices such as biomedical implants. Therefore, ME transducers are an attractive candidate for wireless power transfer (WPT) using low-frequency magnetic fields, which are less harmful to the human body and can penetrate easily through different lossy media. The literature lacks a comprehensive study on the ME transducer as a power receiver in a WPT link. This paper studies the impact of different ME design parameters on the WPT link performance. An accurate analytical model of the ME transducer, operating in the longitudinal-transverse mode, is presented, describing both temporal and spatial deformations. Nine ME transducers with different sizes (ME volume: 5-150 mm³) were fabricated with Galfenol and PZT-5A as magnetostrictive and piezoelectric layers, respectively. Through the modeling and measurement of these ME transducers, the effects of the ME transducer dimension, DC bias magnetic field, loading (R_L) , and operation frequency on the resonance frequency, quality factor, and received power (P_L) of the ME transducer are determined. In measurements, a 150 mm³ ME transducer achieved > 10-fold higher P_L for a wide R_L range of 500 Ω to 1 M Ω at 95.5 kHz, compared to an optimized coil with comparable size and operation frequency.

Index Terms—Biomedical implants, efficiency, inductive coils, low-frequency operation, magnetic field, magnetoelectric transducers, wireless power transfer.

I. INTRODUCTION

WIRELESS power transfer (WPT) can be used in a wide variety of applications that require contactless energy

Manuscript received June 20, 2021; revised August 26, 2021; accepted October 1, 2021. Date of publication October 8, 2021; date of current version December 9, 2021. This work was supported by National Science Foundation (NSF) under Grant ECCS-1904811. This paper was recommended by Associate Editor A. Demosthenous. (Sujay Hosur and Rammohan Sriramdas contributed equally to this work.) (Corresponding author: Mehdi Kiani.)

Sujay Hosur and Mehdi Kiani are with the School of Electrical Engineering and Computer Science, Pennsylvania State University, University Park, PA 16802 USA (e-mail: ssh29@psu.edu; muk42@psu.edu).

Rammohan Sriramdas, Sumanta Kumar Karan, Na Liu, and Shashank Priya are with the Department of Materials Science and Engineering, Pennsylvania State University, University Park, PA 16802 USA (e-mail: rxs1279@psu.edu; skk5867@psu.edu; nzl5265@psu.edu; sup103@psu.edu).

Color versions of one or more figures in this article are available at https://doi.org/10.1109/TBCAS.2021.3118981.

Digital Object Identifier 10.1109/TBCAS.2021.3118981

transfer for either direct powering or battery charging [1]–[3]. In particular, WPT is of paramount importance in implantable medical devices (IMDs) to eliminate their batteries, which results in further miniaturization and an increase of their overall lifetime [4]–[6]. In WPT, delivering the required power with high efficiency within safety limits is key. The most conventional method for WPT is the inductive coupling that operates using magnetic fields [7]–[10].

When the IMD size is in the centimeter (cm) range and the WPT distance is short, multi-coil inductive links (often operating with MHz-range magnetic fields) can deliver a large amount of power (P_L) to a load (R_L) with high power transfer efficiency (PTE) [9]. To further reduce the tissue damage and improve the IMD longevity, it is preferable to miniaturize the IMD to millimeter (mm) scales [11]. To achieve high PTE with mm-scale coils, the operation frequency (f_n) should be increased to several hundreds of MHz or even GHz [12]–[17]. However, WPT links using high-frequency magnetic fields are potentially more harmful to the human body as they cause more tissue heating [18], and therefore, they are strictly limited by the specific absorption rate (SAR) [19]. We showed in [17] that the SAR is proportional to $(f_p \times I_1)^2$, where I_1 is the peak current of the transmitter coil (related to the transmitted power). Therefore, the transmitted power level is strictly limited at higher f_p for a given SAR limit.

For low-frequency WPT to IMDs, a capacitive link that operates with electric fields can be employed. A capacitive WPT link, formed with two pairs of parallel plates (size of each plate: $20 \times 20 \text{ mm}^2$) spaced by > 70 cm, has been developed in [20] to deliver up to $\sim 287 \text{ mW}$ with a PTE of 54% at a powering distance (d) of 5 mm. Despite these promising results with large plates and small d, to the best of our knowledge capacitive links for WPT to small IMDs at large d have not been investigated vet.

Recently, ultrasonic links with a pair of ultrasonic transducers have been studied and developed for WPT to mm-scale IMDs that need to be implanted in deep tissues [21]–[24]. Ultrasonic waves enjoy lower acoustic loss in tissue, smaller wavelength (better focusing capability), and higher safety limits, compared to electromagnetic waves. Despite all their advantages, ultrasonic WPT links suffer from high ultrasound loss in bone and air, sensitivity to ultrasonic transducers' misalignments, and the need for intimate skin contact [25].

1932-4545 © 2021 IEEE. Personal use is permitted, but republication/redistribution requires IEEE permission. See https://www.ieee.org/publications/rights/index.html for more information.

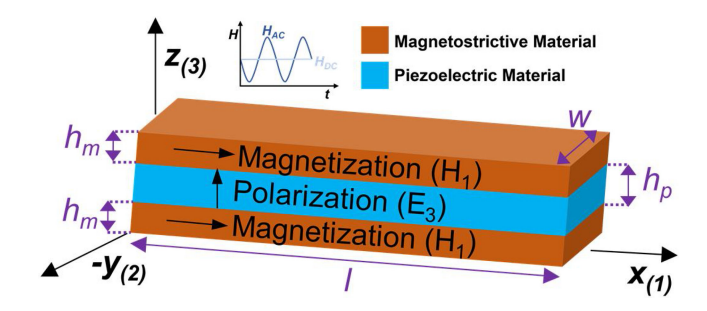


Fig. 1. A conventional ME transducer geometry (and axes convention) with layered magnetostrictive and piezoelectric materials.

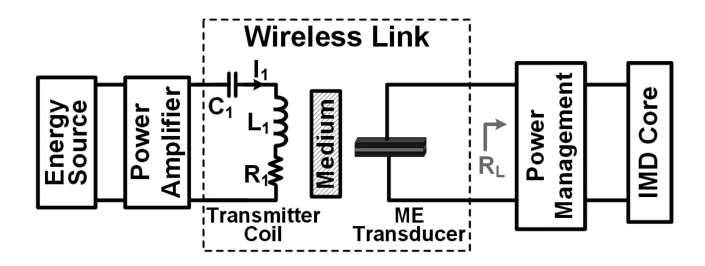


Fig. 2. Generic block diagram of a WPT link for IMDs with a ME transducer as the power receiver.

Over the past decade, magnetoelectric (ME) composites have attracted significant attention for magnetic field sensing and energy harvesting from low-frequency ambient magnetic fields (e.g., 60 Hz) [26]-[30]. In the most common form of ME transducers, magnetostrictive and piezoelectric materials are layered to form a strain-coupled composite as shown in Fig. 1. ME transducers convert an incident AC magnetic field (H_{AC}) into an AC voltage in two steps: 1) The magnetostrictive material generates mechanical strain in response to the applied H_{AC} ; 2) The strain field is converted to electric charge through the piezoelectric layer. An optimal DC bias magnetic field (H_{DC}) is also applied along with H_{AC} as magnetostriction is a second-order effect, and the bias field induces piezomagnetic coupling. For a given operation frequency, electromagnetic waves have much larger wavelengths than acoustic waves. Therefore, small and low-frequency ME transducers are more effective in converting magnetic fields to electric fields as compared to inductive coils [31].

ME transducers can be utilized in WPT with low-frequency magnetic fields, which can penetrate easily through different lossy media. Low-frequency magnetic fields are also safer (less absorption, less heating), thereby allowing more transmitted power. Fig. 2 shows a generic block diagram of a WPT link for IMDs using the ME transducer as the power receiver. An external transmitter coil generates an AC magnetic field, which is converted into an AC voltage by the implanted ME transducer (power management and IMD core are modeled as an equivalent AC load, R_L , for simplicity).

Several groups have so far employed ME transducers for WPT to IMDs [32]–[38]. In [32], a disc-shaped (10 mm diameter) ME transducer has been fabricated and tested at 200

kHz to demonstrate mW-level power delivery with an mTlevel AC field. In [33], [34], the effectiveness of ME and mechano-magnetoelectric (MME) transducers, as a wireless power receiver, has been compared. Their lumped equivalent circuit models have also been developed, concluding that ME transducers generate much higher power density than MME transducers. Two cm-scale ME transducers with Galfenol-PZT and Metglas-PVDF layers (ME area: 1×2 cm²) at 70.7 kHz and 99.3 kHz have been fabricated to verify the model, which has been inaccurate in predicting the received power [33]. In [35]–[37], small ME transducers (ME area: 8-16 mm²) with Metglas and PVDF/ PZT layers have been fabricated to power neurostimulators at \sim 180-250 kHz with 0.5-2 mT AC fields. Specifically, the Metglas-PZT ME transducer (8 mm² area) in [36] can receive 1.35 mW of power at a depth of 3 cm with a 0.55 mT AC field at 250 kHz. Ultrasmall $(250 \times 174 \ \mu m^2)$ self-biased ME transducers with thin-film FeGaB-AlN layers have been demonstrated in [38] for energy harvesting at 2.5 GHz.

Despite these recent efforts, the literature still lacks a comprehensive study and detailed modeling of the ME transducer as a power receiver in a WPT link. Compared with the prior work, the contributions of this paper are: 1) Present an accurate analytical model of the ME transducer, describing both temporal and spatial displacements; 2) Comprehensive study on the effects of the ME transducer dimension, H_{DC} , loading (R_L) , and f_p on the resonance frequency (f_n) , quality factor (Q), and received power (P_L) of the ME transducer through accurate modeling and measurement of 9 ME transducers with different dimensions (ME area: 5-75 mm²; volume: 5-150 mm³); 3) Compare the performance of the ME transducer with an optimized coil of similar volume and frequency in measurements at different alignment and loading conditions. Unlike the lumped model in [33] with fixed Q and piezomagnetic stress constant, it will be shown that these two parameters can change with the ME transducer dimension and H_{DC} , and therefore, an optimization with fixed parameters is not sufficient.

The rest of the paper is organized as follows. The ME analytical model is discussed in Section II. The fabrication process for the ME transducers and the measurement setup are discussed in Section III. The study on the ME transducer design parameters with modeling and measurement results is provided in Section IV, followed by discussion and future work in Sections V and conclusion in Section VI.

II. MAGNETOELECTRIC TRANSDUCER MODELING

The ME transducers in our study consist of a piezoelectric bar sandwiched between two magnetostrictive bars, as shown in Fig. 1. The piezoelectric bar is polarized through the thickness, while the magnetostrictive bars are polarized along the length, resulting in a longitudinal-transverse (L-T) mode of operation of the ME transducer [39]. Fig. 1 also shows the axes convention for our analysis, in which x, y, and z (or 1, 2, and 3) relate to length, width, and thickness of the ME transducer, respectively.

The bar geometry has been analyzed in the literature by constructing a lumped equivalent circuit model [33], [40]. The electromechanical resonance-based modeling of the layered

composite has also been investigated, particularly when the transducer size is smaller than the electromagnetic wavelength [41]. However, the lumped circuit model is inadequate to describe the spatial deformation that occurs along the length of the ME transducer. In this section, both temporal and spatial deformations are described for the ME transducer by coupling the magnetostrictive and piezoelectric effects. Moreover, the effect of variations in the material properties with H_{DC} [42] is explicitly described in the present analysis.

The equations of motion are derived from the constitutive relations, force balance, and boundary conditions of the ME transducer. The stress-strain in the magnetostrictive and piezo-electric materials along the x axis in Fig. 1 are denoted by T_{11m} - S_{11m} and T_{11p} - S_{11p} , respectively. The significant stress and strain components are in the x direction for the L-T mode, and thus, only T_{11} and S_{11} are considered in both piezoelectric and magnetostrictive materials. The AC magnetic field along x in the magnetostrictive material and the AC electric field along z in the piezoelectric material are represented by H_1 and E_3 , respectively. It is assumed that H_1 and E_3 are uniform throughout the respective materials.

The elastic stiffness for the piezoelectric material at a constant electric field, the permittivity at the constant strain in the piezoelectric material, and the elastic stiffness at a constant magnetic field for the magnetostrictive material are denoted by c_{11p}^E , ε_{33p}^S , and c_{11m}^H , respectively. The effective piezoelectric and piezomagnetic stress constants of interest (for the relevant stress components) for the piezoelectric and magnetostrictive materials are e_{31p} and e_{11m} , respectively. The constitutive relations among the significant stress components and the electric displacement D_3 within the composite are given by [43], [44]:

$$T_{11m} = c_{11m}^H S_{11m} - e_{11m} H_1 (1.1)$$

$$T_{11p} = c_{11p}^E \ S_{11p} - e_{31p} E_3 \tag{1.2}$$

$$D_3 = e_{31p} S_{11p} + \varepsilon_{33}^S E_3 \tag{1.3}$$

The length and width of the ME transducer and thickness of the magnetostrictive and piezoelectric bars are denoted by l, w, h_m , and h_p , respectively, as shown in Fig. 1. Let the displacement of the infinitesimal element of length $\mathrm{d}x$ be u(x,t), and the density of magnetostrictive and piezoelectric materials be denoted by ρ_m and ρ_p , respectively. The equation of motion for the displacement of ME transducer using the force balance over $\mathrm{d}x$ employing Newton's second law is derived as [40]:

$$(h_p \rho_p + 2h_m \rho_m) \frac{\partial^2 u}{\partial t^2} = 2h_m \frac{\partial T_{11m}}{\partial x} + h_p \frac{\partial T_{11p}}{\partial x}$$
 (2)

Let us define thickness ratio $\nu=h_p$ / h, where $h=h_p+2$ h_m is the total thickness of the ME transducer. It is assumed that the deformation is uniform throughout the thickness of the composite resulting in a longitudinal strain component given by $\partial u/\partial x$. The solution to (2) is obtained by using the Separation of Variables method employing (1) with the Heaviside step function [45] for both electric and magnetic fields. Let the solution for displacements be written as $u(x,t)=\sum_{i=0}^{\infty}X_i(t)\psi_i(x)$, where $X_i(t)$ is the temporal displacement and $\psi_i(x)$ is the spatial displacement, for the

 i^{th} mode. The assumed modal solutions for the temporal and spatial displacements are X_i $(t) = A_i \cos(\omega_i t) + B_i \sin(\omega_i t)$ and ψ_i $(x) = C_i \cos(\omega_i x/a) + D_i \sin(\omega_i x/a)$ [46], where a is:

$$a = \sqrt{\frac{c_{11p}\nu + c_{11m}(1-\nu)}{\rho_p\nu + \rho_m(1-\nu)}}$$
 (3)

The resonance (or natural) frequency in the i^{th} mode (ω_i) is estimated (neglecting the damping in the structure) as:

$$\omega_i = i\pi a/l; i = 1, 2, 3, \dots \infty \tag{4}$$

To describe the equations of motion succinctly in the fundamental mode of vibration (i=1), the integral $\int_0^l \psi^2 \mathrm{d}x$, temporal displacement, and the resonance frequency are denoted by κ, X , and $\omega_n = 2\pi f_n$, respectively. The magnitude of ω_n is determined using the free-free boundary conditions at x=0 and l for the ME transducer. The voltage developed by the ME transducer, V, is dependent on R_L connected to the ME transducer. From Gauss's law, integrating the (1.3) gives an estimate of the charge and the differential of that is the current flowing through R_L . By substituting temporal and spatial displacements into (2), the governing equations of motion for the ME transducer operating in L-T mode are derived as [47]:

$$M\ddot{X} + C\dot{X} + KX + GV = LH_1 \tag{5}$$

$$V + R_L C_p \dot{V} - R_L G \dot{X} = 0 \tag{6}$$

where, $M = (2h_m \rho_m + h_p \rho_p) w \kappa$, $C = 2\zeta (2h_m \rho_m + h_p \rho_p) w \kappa \omega_n$, $K = (2h_m c_{11m} + h_p c_{11p}) w \kappa \omega_n^2 / a^2$, $G = w e_{31p} \psi |_{x=0}^{x=l}$, $L = 2h_m w e_{11m} \psi |_{x=0}^{x=l}$, and $C_p = \varepsilon_{33}^S w l / h_p$.

The equivalent mass, stiffness, damping coefficient, piezoelectric coupling coefficient, piezomagnetic coupling coefficient, and the piezoelectric layer capacitance are denoted by M, K, C, G, L, and C_p respectively. The type of damping in the composite is assumed to be viscous dissipation with a damping ratio, ζ . It may be noted that $\psi|_x^x = 0$ represents the spatial displacement difference at the boundaries, i.e., $\psi(l) - \psi(0)$. The solution to (5) and (6) is obtained by assuming harmonic excitation for the AC magnetic field as $H_1 = |H| e^{j\omega t}$. The ME transducer voltage and temporal displacement are also harmonic functions represented by $V = |V| e^{j\omega t}$ and $X = |X| e^{j\omega t}$, respectively:

$$|V| = \left| \frac{j\omega GL}{j\omega G^2 + \left(\frac{1}{R_L} + j\omega C_p\right)(K - M\omega^2 + j\omega C)} \right| \times |H|$$
(7)

$$|X| = \left| \frac{L}{\left(\frac{(K - M\omega^2 + j\omega C) + j\omega G^2}{\left(\frac{1}{R_L} + j\omega C_p \right)} \right)} \right| \times |H|$$
 (8)

For simplicity, let us introduce nondimensional parameters: frequency ratio ω/ω_n (operation frequency $\omega=2\pi f_p$), piezoelectric coupling factor $k_p^2=G^2/(MC_p\omega_n^2)$, quality factor $Q\approx 1/2\zeta$, and voltage factor Υ . The amplitude of the open-circuit

voltage $|V_{oc}|$ is obtained by setting $R_L \to \infty$ in (7) and rearranging the terms as:

$$|V_{oc}| = \frac{e_{11m}}{e_{31p}} h |\Upsilon| \times |H|;$$
 (9)

where,

$$|\Upsilon| = \left| \frac{k_p^2 (1 - v)}{1 - \left(\frac{\omega}{\omega_n}\right) + k_p^2 + j\left(\frac{\omega}{\omega_n}\right)/Q} \right|$$

Note that the piezomagnetic stress constant e_{11m} is a function of the applied H_{DC} . Thus, the ME voltage is dependent on both H_{AC} magnitude (|H|) and H_{DC} . It should also be noted that k_p is inherently dependent on the thickness ratio ν . Thus, the voltage factor Υ is an explicit non-dimensional indicator of the voltage generated by the ME transducer as a function of ω and ν for a given Q and provides the range of frequencies, over which the desired voltage can be achieved for a given ν .

The ME transducer's received power, $P_L = |V|^2/2R_L$, can be calculated using |V| in (7) as:

$$P_L = 0.5 \left(h \omega \frac{e_{11m}}{e_{31p}} |H| \right)^2 R_L \rho;$$
 (10)

Where $\boldsymbol{\rho}$ is given by the equation at the bottom of this page.

Using (10), the optimal resistance $(R_{L,opt})$, where P_L is maximized, is given by:

$$R_{L,opt} = \frac{\sqrt{\left(1 - \left(\frac{\omega}{\omega_n}\right)^2\right)^2 + \left(\left(\frac{\omega}{\omega_n}\right)/Q\right)^2}}{\omega C_p \sqrt{\left(\left(\frac{\omega}{\omega_n}\right)/Q\right)^2 + \left(1 - \left(\frac{\omega}{\omega_n}\right)^2 + k_p^2\right)^2}}$$
(11)

With $R_{L,opt}$ from (11), the optimal received power $P_{L,opt}$ from the ME transducer can be found as:

$$P_{L,opt} = \omega_n C_p \left(\frac{e_{11m}}{e_{31p}} h |H| \right)^2 \Pi; \tag{12}$$

where,

$$\begin{split} \Pi &= \frac{k_p^4 \left(\frac{\omega}{\omega_n}\right) (1-\nu)^2 Q^2}{8\sqrt{\left(\left(\frac{\omega}{\omega_n}\right)^2 + Q^2 \left(\left(\frac{\omega}{\omega_n}\right)^2 - 1\right)^2\right) \left(Q^2 \left(1 - \left(\frac{\omega}{\omega_n}\right)^2 + k_p^2\right)^2 + \left(\frac{\omega}{\omega_n}\right)^2\right)}} \\ &= \frac{k_p^4 \left(1-\nu\right)^2 Q^2}{8\sqrt{1+Q^2 k_p^4}} \bigg|_{\omega = \omega_n} \end{split}$$

Replacing device capacitance C_p and k_p in (12) with their aforementioned equations related to the ME transducer dimension, one can find that $P_{L,opt}$ is linearly proportional to the ME transducer width (w) and thickness (h); only for constant ν). It may be noted that both Q and e_{11m} in (12) change with varying

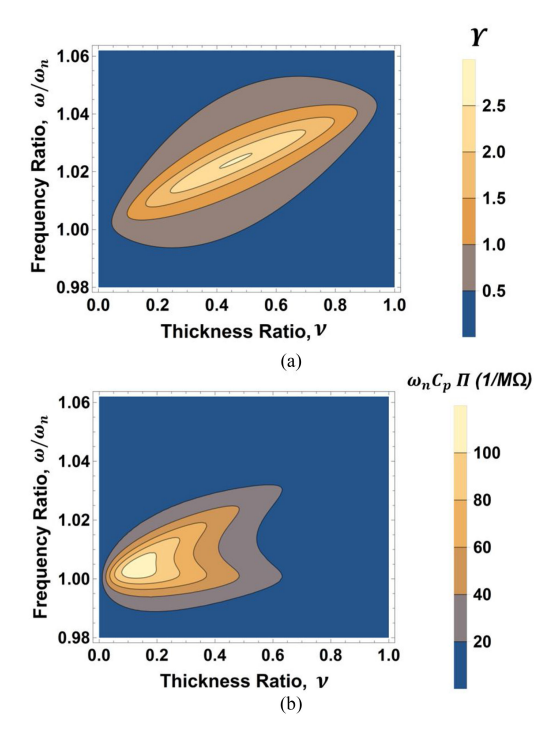


Fig. 3. The effect of frequency ratio (ω/ω_n) and thickness ratio (ν) on the ME transducer (a) voltage factor Υ in (9) and (b) $\omega_n C_p |\mathcal{H}|$ in (12) related to the ME transducer received power. In the model, Q=100, l=15 mm, and w=h=1 mm

the ME transducer dimension, which will also be discussed in detail in Section IV.

Figs. 3a and 3b show the effect of ω/ω_n and $\nu=h_p/h$ on Υ in (9) and $\omega_n C_p \Pi$ in (12), which are related to the ME transducer voltage and received power, respectively. These results are shown for an ME transducer with Q=100, l=15 mm, and w=h=1 mm. Fig. 3a shows that the ME peak voltage occurs at different ω for different ν values. Nevertheless, the absolute maximum voltage is achieved around $\nu=0.5$ (corresponding to $k_p\approx 0.23$) at ω slightly above ω_n ($\omega/\omega_n=1.02$). A similar observation has also been made in [48]. Fig. 3b shows that, unlike the voltage factor (Υ), the absolute maximum of the power-related parameter $\omega_n C_p \Pi$ occurs at the ν range of 0.12-0.19 at ω very close to ω_n . All these conclusions are made with the assumption of constant Q.

III. MAGNETOELECTRIC TRANSDUCER FABRICATION PROCESS AND MEASUREMENT SETUP

For ME transducer fabrication, PZT-5A (PSI-5A4E, Piezo System, Inc.) and FeGa alloy (also known as Galfenol) were used for the piezoelectric and magnetostrictive layers. The fabrication process, shown in Fig. 4a, is as follows. First, the Galfenol was

$$\rho = \frac{\left(1 - \nu\right)^2 k_p^4}{\left(\frac{1}{C_p} - \frac{\left(\omega/\omega_n\right)^2}{C_p} - \frac{\left(\omega/\omega_n\right)^2 \omega_n R_L}{Q}\right)^2 + \left(\omega k_p^2 R_L + \frac{\left(\omega/\omega_n\right)}{Q C_p} + \omega R_L - \left(\left(\frac{\omega}{\omega_n}\right)^2 \omega R_L\right)\right)^2}$$

ME Transducer	Overall Dimension $l \times w \times h$ (mm)	PZT Thickness h _p (μm)	*Cap. <i>C_p</i> (nF)	Quality Factor (Q)	DC Bias Magnetic Field, HDC (Oe)	Optimal Load R_L (k Ω)	Resonance Frequency f _n (kHz)	**Received Power, $P_L(\mu W)$	PTE (%)
ME_{I}	15.01×1.06×0.96	508	0.4	54.3	180	11	100.2	370	0.13
ME_2	14.98×1.09×0.96	196	1	98.8	255	2	98.7	317.1	0.11
ME_3	15.01×1.04×1.01	127	1.43	135.4	295	2	95.1	231.4	0.08
ME_4	4.97×1.03×0.97	508	0.1	34.6	400	1.4	298.1	128.6	0.04
ME_5	5.03×1.06×1.06	196	0.4	71.5	800	1.7	305.6	97.1	0.03
ME_6	4.78×1.03×1.04	127	0.4	100.8	890	1.5	312.2	95	0.03
ME_7	15.08×5.06×2.00	508	1.7	106	790	4.8	95.5	1222.8	0.44
ME_8	15.09×5.10×1.16	196	4.5	112.9	575	0.7	96.8	1728.5	0.62
ME_9	15.05×5.02×1.08	127	7.8	110.4	560	0.2	94.8	1417.5	0.51

TABLE I
SPECIFICATIONS OF THE FABRICATED ME TRANSDUCERS AND THEIR MEASURED CHARACTERISTICS

^{*}DC capacitance of the ME transducer. **Measured using an AC magnetic field (HAC) of 1.41 Oe peak corresponding to an input power of 279 mW.

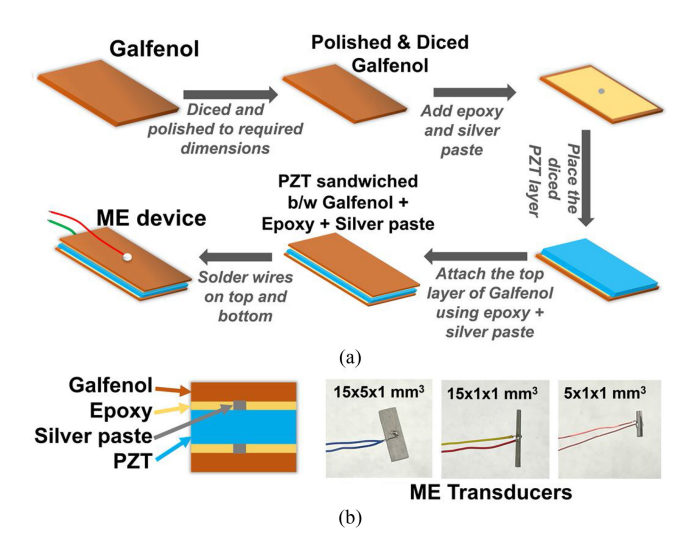


Fig. 4. (a) The step-by-step process for the fabrication of ME transducers. (b) Cross-section view of a fabricated ME transducer along with the images of three of the fabricated ME transducers (out of nine ME transducers).

polished using sandpaper and diced as per required dimensions using a dicing saw. Once cut, the second round of polishing was done using higher grade sandpaper until a relatively smooth surface was achieved. Then, standard PZTs with thicknesses of 508 μm , 196 μm , and 127 μm were cut to the required dimensions using a dicing saw. The PZT layer was then sandwiched between the two polished Galfenol layers having the same length and width. For adhesion between Galfenol and PZT layers, epoxy (DP-460, 3M) was used. To maintain electrical contact between the layers, a dab of silver paste (Leitsilber 200 Silver Paint, Ted Pella) was introduced between the layers. To cure the adhesive, appropriate weights were placed over the sample at room temperature for 18 hours. Since the silver paste cured quicker than the epoxy, there was no mixing of the two, and a good electrical conductivity was ensured among all the layers.

To achieve the required dimensions, the top and bottom Galfenol layers were again polished using a 1200/P4000 grade sandpaper. Finally, for electrical contacts, two copper wires were soldered at the center on top and bottom of the ME transducer, as shown in Fig. 4b. This solder blob was placed at the center to ensure optimal performance. The soldering temperature (300)

°C) was kept below the curie temperature of Galfenol (600 °C) and PZT-5A (360 °C) to prevent any damage to these materials.

To study the effect of different ME design parameters on the WPT link performance, 9 ME transducers with different dimensions were fabricated. Fig. 4b shows the cross-sectional view of the fabricated ME transducer with various layers, and images of three fabricated ME transducers (out of 9). The specifications of all the ME transducers with their measured characteristics are listed in Table I.

These ME transducers can be divided into 4 groups: 1) ME_1 , ME_2 , and ME_3 with a total volume of ~ 15 mm 3 (l=15 mm, w=h=1 mm) and different PZT thicknesses (h_p) of 508 μ m, 196 μ m, and 127 μ m, respectively; 2) ME_4 , ME_5 , and ME_6 with a total volume of ~ 5 mm 3 (l=5 mm, w=h=1 mm) and different h_p s of 508 μ m, 196 μ m, and 127 μ m, respectively; 3) ME_7 with a total volume of ~ 150 mm 3 (l=15 mm, w=5 mm, h=2 mm, $h_p=508$ μ m); 4) ME_8 and ME_9 with a total volume of ~ 75 mm 3 (l=15 mm, w=5 mm, h=1.1 mm) and different h_p of 196 μ m and 127 μ m, respectively.

Fig. 5 shows the experimental setup used to characterize the ME transducers. The ME transducer was placed at the center of the Helmholtz coils, generating a uniform AC magnetic field (H_{AC}) , and a pair of electromagnet coils, generating an adjustable DC bias magnetic field (H_{DC}). The Helmholtz coils, separated by 20 mm and each with 30 mm diameter and 15 turns, were built with a magnet wire (AWG-24) on a 3D-printed plastic frame and holder. The H_{AC} magnitude and frequency were controlled using a signal generator followed by a power amplifier driving the Helmholtz coils. Since the generated magnetic field is linearly proportional to the driving current, an ammeter was used to indirectly measure the H_{AC} magnitude. The H_{DC} was also monitored using a gaussmeter (Model 475, LakeShore, Westerville, OH) by placing its probe close to the center of one of the electromagnets. The voltage across each ME transducer for different R_L values was measured with an oscilloscope and transferred to a computer.

IV. MODELING AND EXPERIMENTAL RESULTS

For modeling each ME transducer, the material properties listed in Table II were used. For more accuracy, the measured Q in Table I was used to calculate the damping ratio ζ for each ME transducer. Since the piezomagnetic constant (e_{11m}) of the

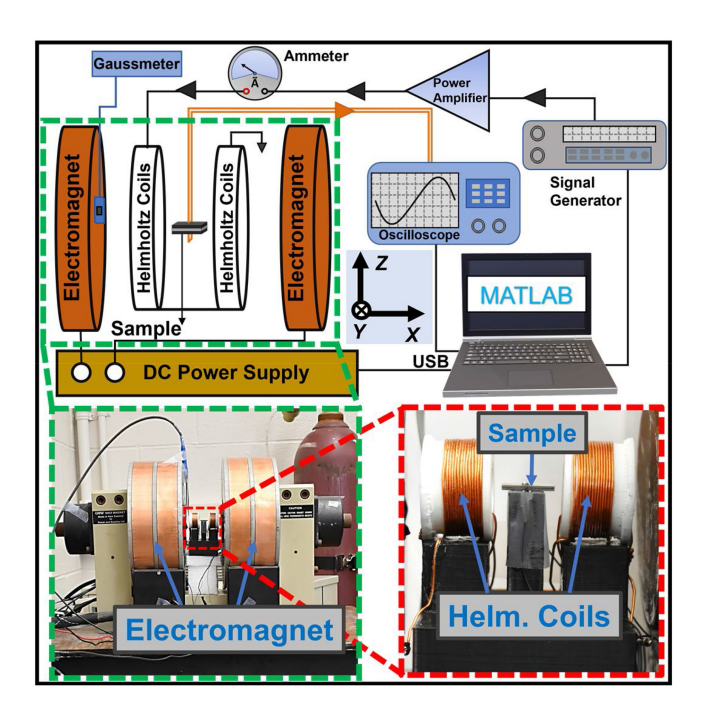
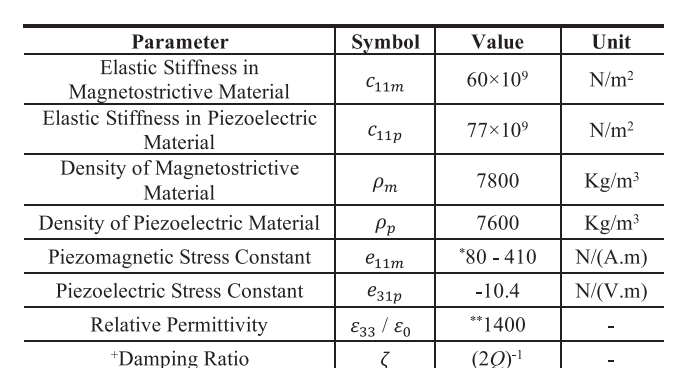


Fig. 5. The experimental setup used for accurate characterization and study of the ME transducers with different dimensions, H_{AC} , and H_{DC} .



 $(2Q)^{-1}$

TABLE II MATERIAL PROPERTIES USED IN OUR MODEL

ME transducer depends on different parameters, such as H_{DC} and dimension, different e_{11m} values were used for different ME transducers (discussed in detail in Section IV.C). Also, (9) and (10) were used to find the modeled resonance frequency f_n (where $|V_{oc}|$ is maximum) and received power P_L of the ME transducer for any given R_L , respectively.

In experiments, the operation of each fabricated ME transducer was first verified by measuring their impedance vs. frequency. Fig. 6a shows the measured impedance profiles (real and imaginary at $H_{DC} = 0$) of ME_{1-3} , which resembles the impedance profile of a PZT transducer with resonance and antiresonance frequencies. All 9 ME transducers showed similar profiles, where the magnitude of the impedance was directly proportional to the thickness of the PZT layer (h_p) . As shown

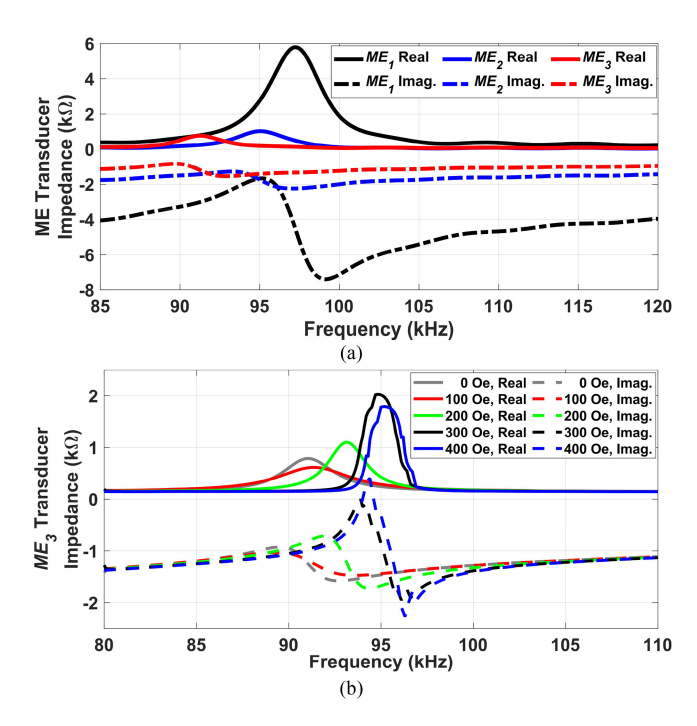


Fig. 6. (a) Measured impedance profile (real and imaginary) of ME_1 , ME_2 , and ME_3 at 0 Oe H_{DC} and whose specifications are listed in Table I. (b) Measured impedance profile (real and imaginary) of ME_3 under different H_{DC} conditions.

in Fig. 6a, ME_1 with the largest $h_p = 508 \mu m$ has the largest impedance at resonance. Fig. 6b shows the measured impedance response of the ME_3 transducer, as an example, at different H_{DC} of 0-400 Oe (1 Oe = 1 G = 100 μ T in air). Thus, H_{DC} can affect the impedance profile of an ME transducer.

Using the setup in Fig. 5, initially two experiments were performed for each ME transducer. In both experiments, the H_{AC} magnitude was fixed at 1.41 Oe at the center of the Helmholtz coils, where the ME transducer was placed. Based on the Helmholtz coils specifications, it was estimated that an AC peak current of 431.3 mA (input power P_{in} of 279 mW) would generate approximately the required peak H_{AC} of 1.41 Oe across all measured frequencies.

In the first experiment, both H_{DC} value and H_{AC} frequency (called operation frequency, f_p , hereafter) were swept for each ME transducer, and the open-circuit voltage of the ME transducers (V_{oc}) was measured. The H_{DC} was varied from 30 Oe to 1000 Oe in steps of 45 Oe (the step size was reduced to 15 Oe in the vicinity of each ME transducer's f_n). At each H_{DC} , the V_{oc} amplitude ($|V_{oc}|$) was measured for a 10 kHz bandwidth near f_n with 100 Hz resolution. This experiment gives insight into how H_{DC} affects $|V_{oc}|$, f_n , and Q of the ME transducer, and determined the H_{DC} for each ME transducer in our studies. Fig. 7 shows the results of this experiment ($|V_{oc}|$ vs. f_p at different H_{DC}) for ME_1 , indicating that H_{DC} affects all three $|V_{oc}|, f_n$, and Q values. For instance, the largest $|V_{oc}|$ was achieved at 180 Oe with $f_n = 100.4 \text{ kHz}$ (ME_1).

In the second experiment, each ME transducer was loaded by a resistance R_L , and the voltage across R_L was measured at

^{*}Different value for each ME transducer (details in Section IV.C).

^{**} At constant strain. + Calculated from measured O

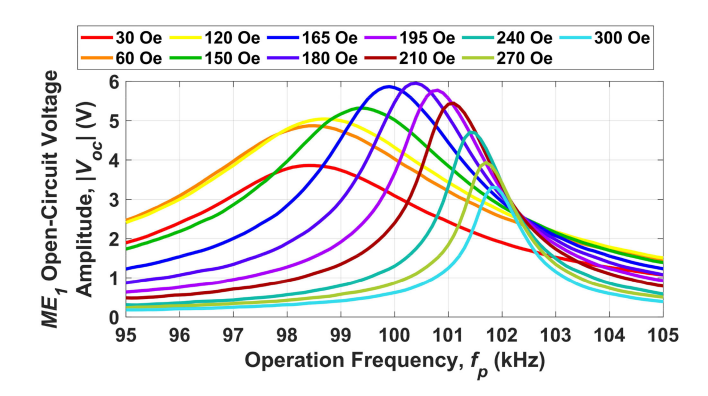


Fig. 7. Measured amplitude of the open-circuit voltage ($|V_{oc}|$) of ME_1 vs. the operation frequency (f_p) for different H_{DC} values, showing the effect of H_{DC} on $|V_{oc}|$, f_n , and Q of the ME transducer ($H_{AC,peak}=1.41$ Oe).

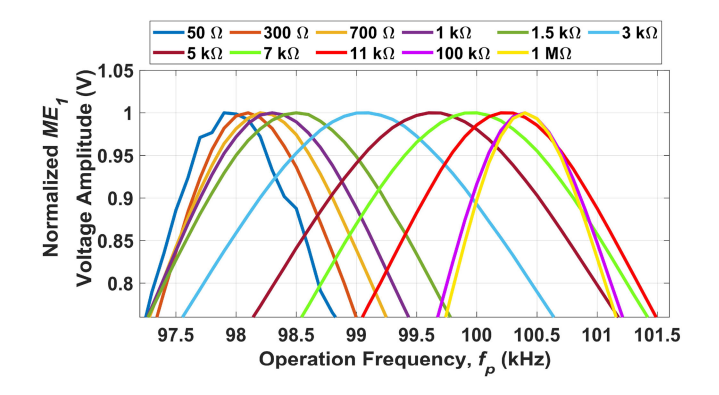


Fig. 8. Measured voltage amplitude of ME_1 (normalized) vs. the operation frequency (f_p) for different R_L values, indicating that increasing R_L can also increase the optimal f_p of the ME transducer.

different f_p , using the H_{DC} values that maximized $|V_{oc}|$ in the first experiment. This experiment helps to understand the effect of R_L on the optimal f_p of the ME transducers, and also provided the optimal f_p at each R_L for each ME transducer in our studies. Fig. 8 shows the measured normalized ME_1 voltage amplitude vs. f_p at different R_L . The optimal f_p increased from 97.9 kHz to 100.4 kHz by increasing R_L from 50 Ω to 1 M Ω , indicating the need to operate at optimal f_p for a given R_L .

In the following subsections, modeling and measurement results will be used to study the effect of the ME transducer dimension, H_{DC} , and R_L on the f_n (and optimal f_p), Q, and P_L of the ME transducer. The discussion is presented in a way that a designer could optimize an ME transducer as the power receiver in a WPT link for a given application.

A. Effect of DC Bias Magnetic Field and Loading on Resonance Frequency and Optimal Operation Frequency

When operating the ME transducer in L-T mode, it is well established that its resonance frequency f_n is inversely proportional to its overall length (l), as also seen in (4) [35]. As shown in Table I, ME_{1-3} and ME_{7-9} with approximately similar l=15 mm achieved f_n in the range of 94.8-100.2 kHz, while ME_{4-6}

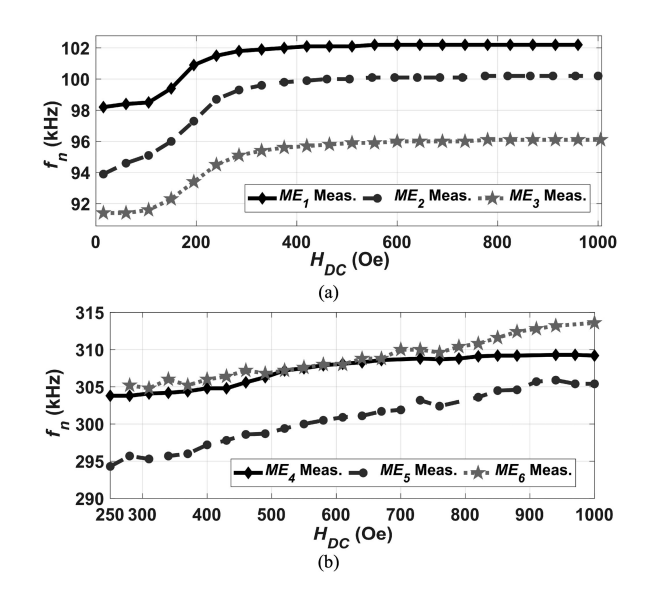


Fig. 9. Measured results of the resonance frequency f_n vs. H_{DC} of (a) ME_{1-3} with l=15 mm and (b) ME_{4-6} with l=5 mm.

with reduced l=5 mm achieved higher f_n in the 298.1-312.2 kHz range (there are slight variations in l due to fabrication limitations). This indicates that reducing l by 3-fold increases f_n by almost the same factor. Apart from l, H_{DC} can also affect the f_n of the ME transducer. Fig. 7 shows these effects for ME_1 .

To further illustrate this effect, Figs. 9a and 9b show the measured f_n values vs. H_{DC} for ME_{1-3} (l=15 mm) and ME_{4-6} (l=5 mm). In all measurements, the frequency, at which the ME transducer generated the highest $|V_{oc}|$, was considered as f_n at that H_{DC} . The measured f_n values slightly increased with H_{DC} and then saturated at large H_{DC} values of ~ 400 Oe for ME_{1-3} and 900 Oe for ME_{4-6} . This phenomenon of increasing and saturation of the f_n is due to the variation in the elastic stiffness of the magnetostrictive material (c_{11m}), which is known to be a function of H_{DC} [49].

The modeled and measured results in Figs. 10a and 10b for ME_{1-3} and ME_{4-6} , respectively, show that the optimal f_p for driving ME transducers also slightly increased with R_L and then saturated at large R_L . For instance, ME_1 achieved measured optimal f_p of ~ 98.2 kHz for $R_L < 1$ k Ω , and optimal f_p increased to ~ 100.4 kHz for $R_L > 20$ k Ω (Fig. 10a). Or ME_5 achieved measured optimal f_p of ~ 301.1 kHz for $R_L < 200$ Ω , and optimal f_p increased to ~ 305.6 kHz for $R_L > 1$ k Ω (Fig. 10b). The modeled and measured optimal f_p values match well for all ME transducers. The slight discrepancy (up to 6.7%) could potentially be due to the material property variations and imperfections involved in fabrications and measurements.

These results reveal that the ME transducer's f_n can change at different H_{DC} , and the optimal f_p for driving ME transducers at different R_L could be different. Thus, one should sweep frequency to find the optimal $f_p = f_n$ for a given H_{DC} and R_L . Since this eventually affects ME transducer's P_L , an optimization in three dimensions of H_{DC} , R_L , and f_p is needed.

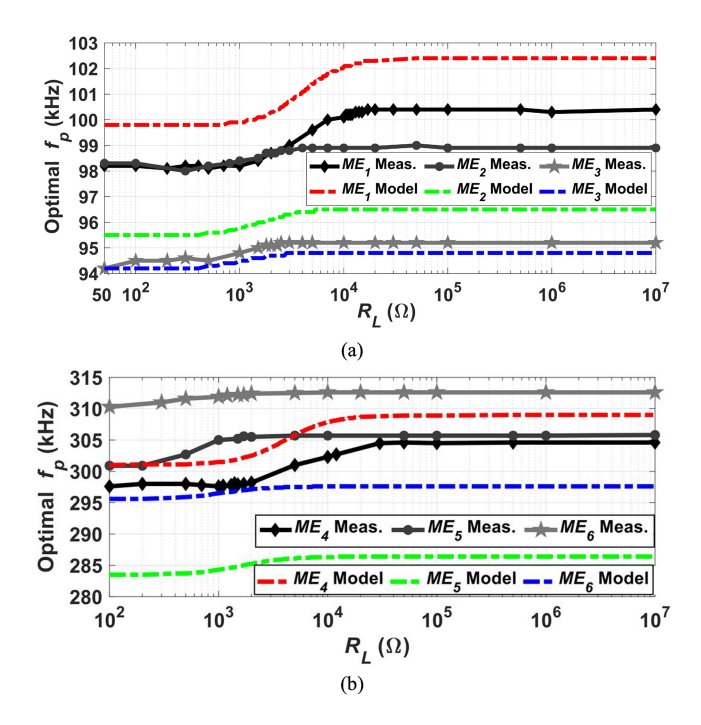


Fig. 10. Modeled and measured optimal f_p (for driving ME transducers) at different R_L of (a) ME_{1-3} with l=15 mm and (b) ME_{4-6} with l=5 mm.

B. Effect of Dimension and DC Bias Magnetic Field on Quality Factor

The quality factor Q of the receiver in a WPT link has a considerable impact on the link's bandwidth, optimal loading, and more importantly PTE [9]. The Q of small ME transducers is significantly high (compared to small coils), particularly at low frequencies (Table I) [17]. It is important to study the effect of design parameters, such as dimension and H_{DC} , on the Q of the ME transducer. Table I lists the measured unloaded Q of all ME transducers at optimal H_{DC} and f_n .

The Q was calculated as the ratio of measured f_n to the half-power bandwidth. Table I implies that for the same overall ME thickness (h=1 mm) in ME_{1-3} or ME_{4-6} , decreasing the PZT thickness (h_p) increases the Q. But this could be misleading as P_L in Table I shows an opposite trend, i.e., the higher h_p led to higher P_L in ME_{1-3} or ME_{4-6} . This is due to the changes in the piezomagnetic stress constant (e_{11m}), which also depends on the dimension (discussed in Section IV.C). Thus, one should be careful in relating the Q of ME transducers to their capability in receiving power.

Fig. 11 shows the effect of H_{DC} on the measured Q of ME_{1-6} . The Q increased with H_{DC} and then saturated at very large H_{DC} . For instance, the Q of ME_2 started to increase from ~ 20 to 200 for H_{DC} increase from ~ 150 Oe to 600 Oe and beyond (Fig. 11a). Or the Q of ME_4 started to increase from ~ 45 to 100 for H_{DC} increase from ~ 400 Oe to 700 Oe and beyond (Fig. 11b). This increase in Q with H_{DC} is due to the increase in tensile stresses within the ME transducer [50]. From Fig. 11, one would prefer to operate the ME transducer at higher H_{DC} where the Q is higher. However, the piezomagnetic stress constant e_{11m} also changes with H_{DC} . Thus, both Q and e_{11m} should

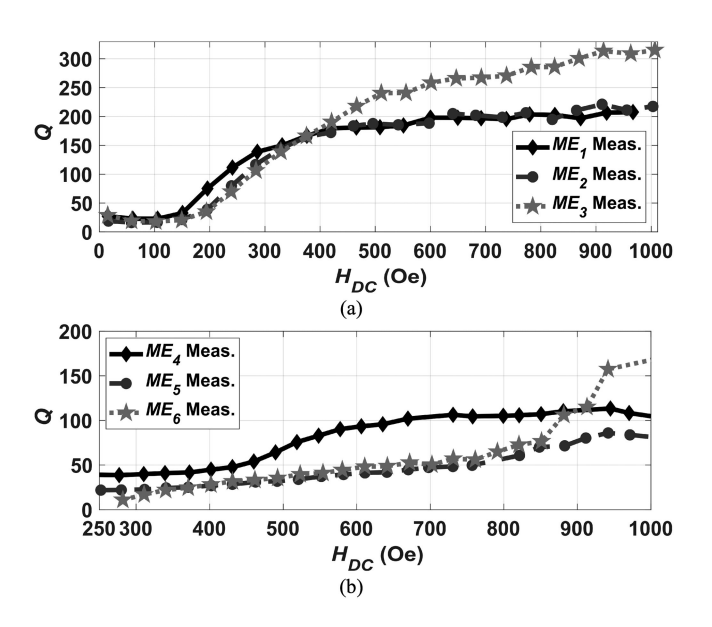


Fig. 11. Measured Q of (a) ME_{1-3} and (b) ME_{4-6} at different H_{DC} values.

be considered in the optimization of H_{DC} , which is detailed in the following sub-section.

C. Effect of DC Bias Magnetic Field, Operation Frequency, ME Dimension, and Loading on Received Power

In a WPT link, the receiver should be able to capture the maximum power (P_L) . Conventionally, the parameters that affect P_L are the receiver dimension, f_p , and R_L . For the ME transducer as a power receiver (shown in Fig. 2), H_{DC} can also affect P_L in addition to dimension, f_p , and R_L . Therefore, the effects of these parameters on the P_L of the ME transducer are studied for an incident H_{AC} of 1.41 Oe peak.

Figs. 12a and 12b show the measured peak open-circuit voltage $|V_{oc}|$ of the ME_{1-3} and ME_{4-6} at different H_{DC} values, respectively. At each H_{DC} , the maximum $|V_{oc}|$ for the optimal f_n was measured (as discussed in Fig. 7). Fig. 12 indicates that peak $|V_{oc}|$ of each ME transducer is maximized at an optimal H_{DC} , in which the piezomagnetic coupling is maximum. The optimal H_{DC} depends on the ME transducer's geometry (particularly its magnetostrictive material thickness h_m), and it increases with h_m . For example, the measured optimal H_{DC} for ME_1 with h_m of $\sim 250~\mu m$ was 180 Oe, while ME_3 with the same volume but larger h_m of $\sim 437~\mu m$ required the optimal $H_{DC}=295$ Oe (Fig. 12a). A similar trend can also be seen for ME_{4-6} in Fig. 12b.

Figs. 13a and 13b show the modeled and measured P_L of the ME_{1-3} and ME_{4-6} at different f_p using the H_{DC} and R_L values in Table I, respectively. For each ME transducer, the peak P_L values from modeling and measurement matched very well, but they occurred at slightly different f_p as described previously in Fig. 10. Fig. 13 shows the importance of operating at the optimal f_p to achieve the highest P_L .

Figs. 14a and 14b show the modeled and measured P_L of ME_{1-3} and ME_{4-6} for different R_L using H_{DC} values in Table I and optimal f_p in Figs. 10a and 10b. The peak P_L was observed at

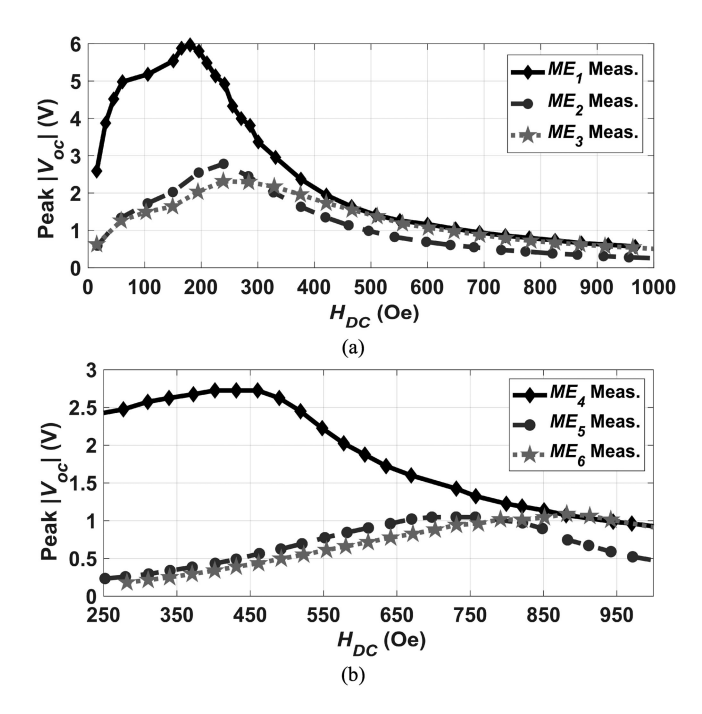


Fig. 12. Measured peak open-circuit voltage $|V_{oc}|$ of (a) ME_{1-3} and (b) ME_{4-6} at different H_{DC} values ($H_{AC,peak}=1.41$ Oe).

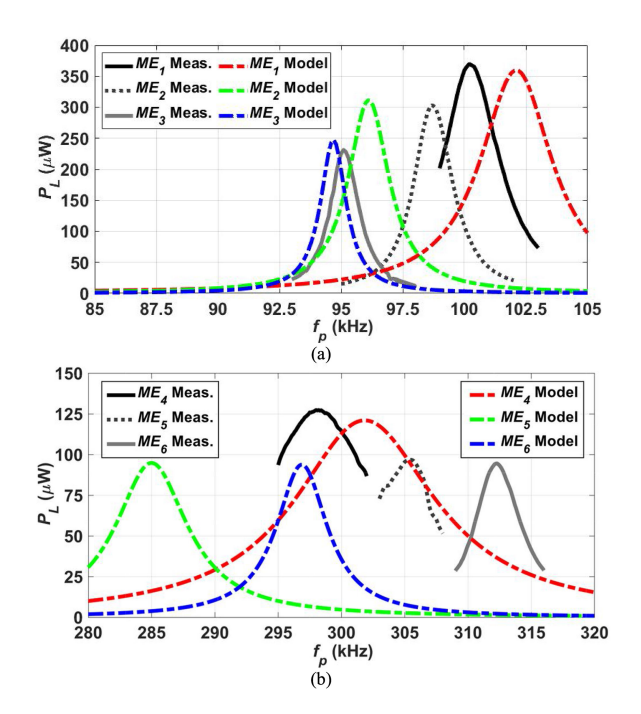


Fig. 13. Modeled and measured received power P_L of (a) ME_{1-3} and (b) ME_{4-6} for different f_p using H_{DC} and R_L values in Table I ($H_{AC,peak}=1.41$ Oe).

an optimal R_L for each ME transducer. Some transducers, such as ME_1 , showed two peaks for P_L (Fig. 14a), resulting from the high piezoelectric coupling factor for the ME transducer compared to the mechanical damping ratio [51]. The modeled and measured P_L values matched very well for most ME transducers, showing the accuracy of our model. There is some discrepancy

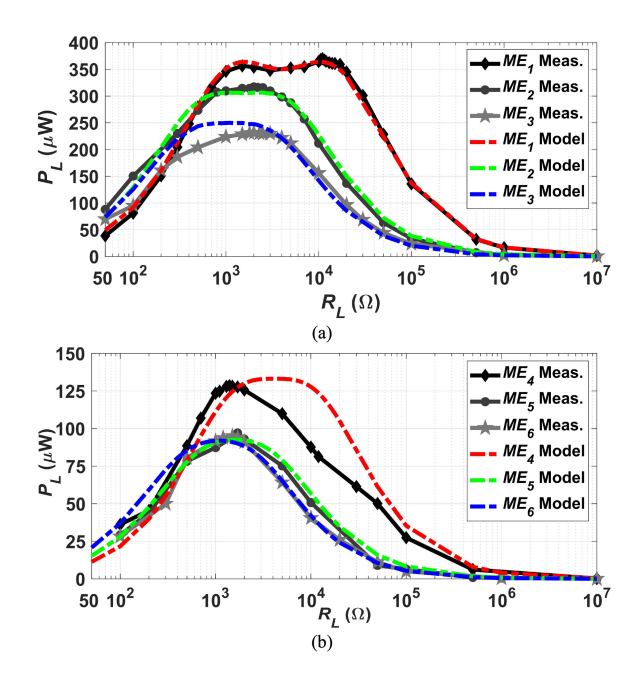


Fig. 14. Modeled and measured received power P_L of (a) ME_{1-3} and (b) ME_{4-6} for different R_L using their H_{DC} values in Table I and optimal f_p values in Fig. 10 ($H_{AC,peak} = 1.41$ Oe).

for ME_4 that could potentially be due to the variation of material properties and fabrication or measurement imperfections, which is evident from its low Q.

Fig. 14 also shows that ME transducers can achieve high P_L for a wide R_L range. For instance, ME_1 and ME_4 with different dimensions could achieve > 50% of their peak P_L of 370 μ W and 128.6 μ W for wide R_L ranges of ~ 0.25 -75 $k\Omega$ and ~ 0.35 -30 $k\Omega$, respectively.

For simplicity, the H_{DC} for each ME transducer in Table I was determined based on peak $|V_{oc}|$ with infinite R_L (Fig. 12). However, as shown in Fig. 6b, the impedance profile of the ME transducer can change with H_{DC} . Therefore, the optimal H_{DC} that maximizes P_L can vary with R_L . For example, by reducing the H_{DC} of ME_3 from 295 Oe to 230 Oe, its P_L was increased by $\sim 45\%$ at $R_L=2$ k Ω thanks to better impedance matching. Thus, for achieving the highest possible P_L one needs to find the optimal H_{DC} at a given R_L .

Table I lists the optimal P_L values and PTEs of all ME transducers with different dimensions $(l \times w \times h)$, from which several lessons can be learned. First, P_L is almost linearly proportional to the ME transducer width (w), as the model predicted. For example, for the same PZT thickness (h_p) of 127 μ m, h=1 mm, and l=15 mm, ME_g with larger w of 5 mm achieved \sim 6-fold higher $P_L=1.4$ mW compared with $P_L=231.4$ μ W in ME_g with w=1 mm. Note that ME_g and ME_g have comparable piezomagnetic stress constant e_{11m} of 130 N/A.m and 112.2 N/A.m and Q of 110.4 and 98.8, respectively. Thus, the model prediction was accurate.

Second, comparing P_L values of ME_2 and ME_5 (or ME_3 and ME_6) with almost similar h_p , h, and w but different l ($l_{ME2,3} = 15$ mm vs. $l_{ME5,6} = 5$ mm) and thereby different f_n reveals that P_L also changed with l (or f_n). This is mainly due to the

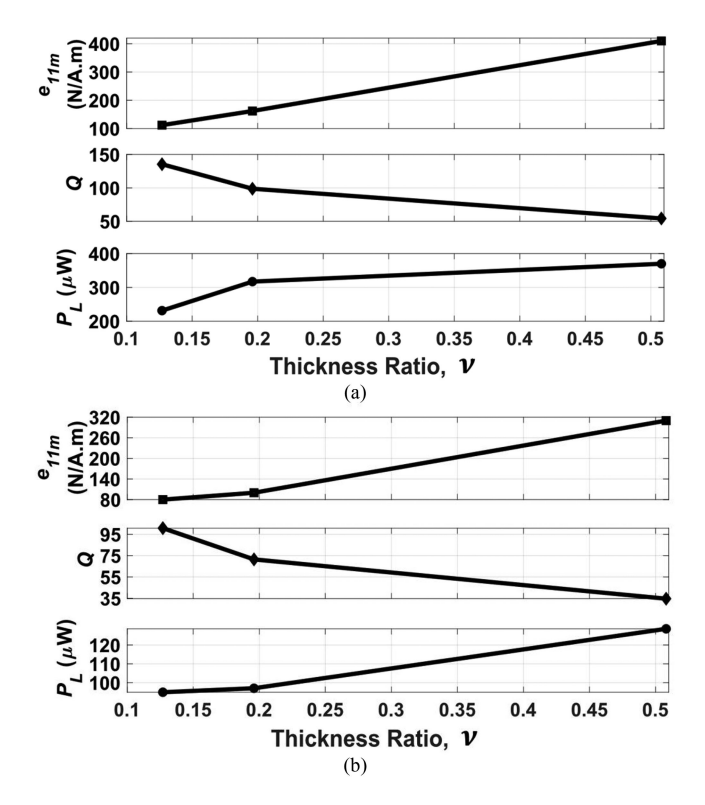


Fig. 15. Estimated piezomagnetic stress constant e_{11m} , measured Q, and measured P_L at different thickness ratios (ν) for (a) ME_{I-3} and (b) ME_{4-6} .

difference in e_{11m} (e.g., $e_{11m,ME2} = 162$ N/A.m and $e_{11m,ME5} = 100$ N/A.m), which will be explained later in Fig. 15. Thus, assuming constant e_{11m} in the model for different l could be misleading.

Third, comparing P_L values of $ME_{8,9}$ and ME_7 with ME volumes of $\sim 75~\rm mm^3$ and $150~\rm mm^3$, respectively, suggests that increasing the total ME volume with h not necessarily improves P_L (note that thickness ratio ν is different in ME_{7-9}). Thus, it is important to study the effect of h on P_L . Since the input power remained constant for characterizing all 9 ME transducers (i.e., $P_{in} = 279~\rm mW$), these discussions about P_L can be extended to PTE as well.

Table I shows that within three sets of transducers, ME_{1-3} , ME_{4-6} , and $ME_{8,9}$, with $l \times w \times h$ of $\sim 15 \times 1 \times 1$ mm³, $5 \times 1 \times 1$ mm³, and $15 \times 5 \times 1$ mm³, respectively, P_L increased with h_p . To evaluate the thicknesses of piezoelectric and magnetostrictive layers (h_p and h_m) relative to each other, Figs. 15a and 15b show the estimated (confirmed with measurements) e_{11m} , measured Q, and measured P_L at different $\nu = h_p / (h_p + 2h_m)$ for ME_{1-3} and ME_{4-6} , respectively. Three lessons can be learned from Fig. 15. First, with increasing ν (decreasing h_m) in ME transducers, e_{11m} also increased. As h_m decreases, the magnetic induction occurs at a lower H_{DC} , which can be seen from optimal H_{DC} values in Table I. Second, ME_2 and ME_5 (or ME_3 and ME_6) with similar ν but different $l_{ME2,3} = 15$ mm vs. $l_{ME5,6} = 5$ mm showed different e_{11m} of 162 and 100 N/A.m (or 112 and 80 N/A.m), i.e., l also affected e_{11m} . And third, the effect of Q and e_{11m} on P_L should be considered together. Fig. 15 shows that

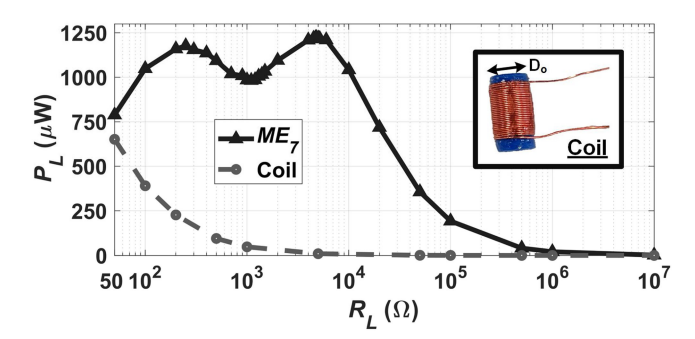


Fig. 16. Measured received power P_L vs. R_L of ME_7 in Table I and an optimized solenoid coil with similar volume of 150 mm³ ($H_{AC,peak}$ = 1.41 Oe).

the measured Q of ME_{1-3} and ME_{4-6} reduced by increasing ν , but P_L increased mainly due to the higher e_{11m} at larger ν .

The results in Fig. 15 are different from what our model predicted in Fig. 3b (i.e., highest $\omega_n C_p \Pi$ for ν range of 0.12-0.19) because Q was assumed to be constant in the model (Q=100) while changing ν . However, comparing ME_{7-9} with almost similar Q in Table I reveals that $ME_{8,9}$ (volume: $\sim 75 \text{ mm}^3$) with ν of 0.12-0.17 achieved higher P_L (1.7 mW, 1.4 mW) than that of ME_7 (1.2 mW) with higher ν of 0.25, even though ME_7 has larger volume of $\sim 150 \text{ mm}^3$. It should also be noted that using correct values of Q and e_{11m} in our model for ME_{1-6} resulted in accurate P_L values in Fig. 14. Therefore, our model with correct Q and e_{11m} (from measurements) can be used to accurately optimize ME transducers.

D. Effect of Misalignment and Surrounding Tissue Medium in Comparison With Inductive Coil

To show the advantage of small ME transducers in converting low-frequency magnetic fields to electric fields in comparison to inductive coils (with comparable size and frequency), the performance of the ME_{7} transducer in terms of its received power, effect of the surrounding tissue medium, and misalignment conditions are discussed here.

Using our design procedure for optimizing inductive links in [17], a wire-wound solenoid coil (Fig. 16 inset) was optimized with HFSS (Ansoft, Pittsburgh, PA). For a fair comparison to ME_7 with $l \times w \times h$ of $\sim 15 \times 5 \times 2 = 150$ mm³ (Table I), the coil diameter (D_o) and volume were limited to 5 mm and 150 mm³, respectively. Following the design flowchart in [17], the wire width (w_c) and the number of turns (n) of the coil were optimized to maximize k^2Q (i.e., maximizing received power), where k is the coupling coefficient (considering the Helmholtz coils in Fig. 5 as the transmitter) and Q is the quality factor of the receiver coil. The optimal $w_c = 0.22$ mm and n = 31 were found. The coil was fabricated with the closest magnet wire (AWG-31) on a 3D-printed plastic frame. To resonate the coil with a measured inductance of 3.34 μ H at 91.8 kHz (close to f_n = 95.5 kHz of ME_{γ}), a 1 μ F capacitor was connected in parallel. The measured impedance at resonance was 7.75 Ω .

Using the setup in Fig. 5, the received power P_L of both ME_7 and coil was measured for different R_L from 50 Ω to 10 M Ω

at $H_{AC, peak}$ of 1.41 Oe. Fig. 16 shows that for the R_L range of 1 k Ω to 100 k Ω (typical implant power range: \sim 0.1-10 mW), ME_{γ} could harvest at least 20-fold higher power than the coil. For instance, at $R_L=1$ k Ω , ME_{γ} and coil achieved P_L of 984.8 μ W and 48.4 μ W, respectively, while the available power from them was 1.22 mW and 1.4 mW. Furthermore, at $R_L=1$ k Ω , ME_{γ} and coil achieved measured PTE of 0.34% and 0.02%, respectively. This shows that for given device size, ME transducers can harvest much higher power at low frequencies, and they can potentially outperform coils even more as the size and frequency are both reduced.

The low P_L of the coil is mainly due to its small 7.75 Ω impedance at resonance, which is challenging to match to a large R_L in a small implant [17]. The resonant impedance of a mm-sized coil (and its link PTE) can be improved by increasing its f_p at the cost of elevated SAR values (more heat dissipation in tissue) and limited allowable transmitted power (discussed in Section V). Also, adding a magnetic core to a mm-sized coil can further increase its PTE and P_L [52].

To verify the effect of the surrounding tissue medium on the ME transducer, P_L at different R_L and Q were measured in the presence of tissues. A piece of chicken breast was wrapped with a thin piece of plastic, and the ME transducer was placed inside it. The average thickness of the tissue on the top/bottom and sides of the ME transducer was 6.5 mm and 2.5 mm, respectively. In all measurements with the tissue, P_L and Q only changed < 10% and < 7.5%, respectively, compared to those in air. Since there is negligible attenuation of low-frequency magnetic fields by the tissue, such slight losses are most likely attributed to the solid loading of the tissue on the ME transducer. This should further be studied in future and potentially be avoided by proper design of the IMD's package.

Since our ME transducers operate in the L-T mode, for optimal performance the face of the Helmholtz coils needs to be perpendicular to the length of the ME transducer, i.e., ME transducer should be along the x axis as shown in Figs. 1 and 5. This also applies to the coil for the maximum flux to pass through it. Therefore, for any misalignment in the form of ME transducer (or coil) rotation along the x axis, P_L did not change in our measurements, as expected. But for rotation of the ME transducer (or coil) for the angle of θ in the xy plane in Figs. 1 and 5, such that $\theta = 0^{\circ}$ and 90° results in $ME_{\gamma}/coil$ along the x and y axes, respectively, P_L drastically reduced for both ME_{γ} and coil. Fig. 17 shows the measured P_L ($R_L = 4.8 \text{ k}\Omega$) for both ME_{γ} and coil vs. different θ , indicating that P_L dropped by \sim 15-fold for both ME_{γ} and coil when θ was changed from 0° to 60° . However, for small θ of $< 45^{\circ}$, ME_{γ} performed better than the coil. For example, P_L dropped by 2.2 times in ME_7 vs. 3.6 times in coil at $\theta = 30^{\circ}$.

V. DISCUSSION AND FUTURE WORK

Since ME transducers operate based on both DC and AC magnetic fields (H_{DC} and H_{AC}), compliance with different safety limits is needed. Based on the IEEE standard [19], the dosimetric reference limit (DRL) of 167 mT (corresponding to 1670 Oe) is the maximum allowable H_{DC} . All the ME transducers in Table I

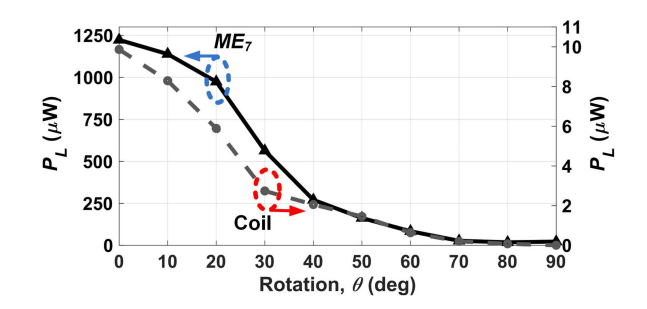


Fig. 17. Measured received power P_L of ME_7 and solenoid coil vs. angle of rotation (θ) in the xy plane in Figs. 1 and $5(H_{AC,peak}=1.41 \text{ Oe})$.

require H_{DC} well below this limit (highest H_{DC} is 890 Oe for ME_6).

For the maximum allowable H_{AC} at 100 kHz $\leq f_p \leq 5$ MHz (the case in this work), there are two IEEE limits: one for avoiding electrostimulation, which is the DRL limit of $0.209\times10^{-3}\times f_p$ V/m, and one for tissue heating, which is the SAR limit of 2 W/kg [19]. It has already been shown in [36] that at $f_p = 250$ kHz and depth of 30 mm inside soft tissue (indicating ME transducer's viability for deep implants), H_{AC} of 550 μ T rms (~ 7.78 Oe peak) is permissible under the DRL limit. Our measurements were conducted with the H_{AC} of 100 μ T rms (1.41 Oe peak). Thus, at an implant depth of 30 mm, our reported P_L values for each ME transducer in Table I could potentially be ~ 25 -fold higher by increasing the H_{AC} if the DRL is concerned. Obviously, the WPT distance (i.e., implant's depth) can further be increased if the required P_L is lower for each ME transducer in Table I.

The average SAR over a volume of 10 g tissue (based on the standard) was also simulated in HFSS using the Helmholtz coils in our setup. At $f_p = 100$ kHz and H_{AC} of 1.41 Oe peak, the simulated SAR was as low as $\sim 19.3 \,\mu\text{W/kg}$ ($<< 2 \,\text{W/kg}$ limit). Thus, DRL is the main safety limit for the ME transducers in this work. The SAR was also simulated with our optimized transmitter coil in [17] at $f_p = 100$ MHz, which is the low-end frequency for miniaturized coils. When the coil was spaced 2 mm from tissue, H_{AC} should be below 39.2 μ T rms (0.55 Oe peak) to limit the SAR at 2 W/kg at 100 MHz. Also, it has been shown in [36] that the allowed magnetic field inside the body at a depth of 30 mm is 30 μ T rms at f_p of 13.56 MHz. Thus, the allowable transmitted power is drastically lower at higher f_p s (even with elevated SAR). This can significantly limit the implant's P_L , which may even be more important than PTE when the implant is miniaturized [17]. This shows the advantage of ME transducers for WPT using low-frequency magnetic fields.

For optimizing the ME transducer as the power receiver, our results suggest the following process. First, one should measure the piezomagnetic stress constant (e_{11m}) of the magnetostrictive material and the quality factor (Q) of the piezoelectric material (preferably loaded with adhesive and magnetostrictive layers) for a range of their dimensions (l, w, h) and H_{DC} . The limited measured values of e_{11m} and Q can be extrapolated and fed into our model in Section II. Then, P_L in (10) is used to sweep the ME transducer geometry (l, w, h_p, h_m) , considering

constraints from application and fabrication, to maximize P_L at a given R_L with highest possible H_{AC} imposed by the DRL limit of $0.209\times10^{-3}\times f_p$ V/m up to frequencies $(f_n\propto 1/l)$ at which the increased SAR reaches 2 W/kg. This ensures that both the optimal ME transducer geometry and the highest allowable transmitted power are achieved, significantly improving P_L .

To realize functional IMDs with ME transducers, additional steps for packaging the IMD, transforming the experimental setup in Fig. 5 into a battery-operated wearable system, and providing H_{DC} without the electromagnet are necessary for future. Similar to ME-based devices in [35], IMDs with electronics, electrodes, and PZT-based ME transducers must be encapsulated with biocompatible materials, such as parylene-C or PDMS [24]. This can also avoid direct contact of toxic PZT with surrounding tissue. Our preliminary measurements show minimal to no change in the response of ME transducers coated with parylene-C or PDMS. In the future, alternative biocompatible piezoelectric materials, such as BaTiO₃ or AlN, can also be used instead of PZT at the cost of lower P_L . It is worth mentioning that the small ME transducers fabricated with AlN in [31] have still outperformed coils.

A battery-operated system in the form of a wearable belt has recently been demonstrated in [53] for operating ME transducers. The wearable unit includes a small permanent magnet for H_{DC} generation, and a coil driven by a power amplifier for generating the required H_{AC} . One can also package the ME transducer with a small hard neodymium magnet as shown in [35]. It is worth noting that the ME response can also be achieved without the use of a hard magnet using self-biased ME composites. The non-zero ME response at zero H_{DC} could arise from intrinsic magnetization hysteresis [54] or an exchange coupling magnetic field [55]. For example, a self-biased thin-film ME transducer with a high Q of 930 has been fabricated in [31] with H_{DC} elimination.

Finally, depending on the power requirement, implant's size, and implantation depth, ME transducers as power receiver can be used in a wide variety of IMD applications. For instance, small ME transducers have already been used for powering (multisite) neural stimulation and recording systems in [32], [35]–[38]. In general, miniaturized IMDs for sensing and actuation applications (e.g., recording and stimulation) in both the central and peripheral nervous systems can benefit from low-frequency ME transducers for mW-level power delivery at short distances (several mm) and sub-mW-level power delivery at large distances (several cm) [56]–[58]. Our future work includes the use of ME transducers for wireless power delivery to small gastric implants [57]. In [36], it has been shown that an ME transducer does not affect MRI scanning, while there could be potential remnant imaging effects in the vicinity of the ME transducer.

VI. CONCLUSION

A comprehensive study on different characteristics of the ME transducer as a power receiver in a WPT link was presented. An analytical model of the ME transducer, consisting of a piezoelectric bar sandwiched between two magnetostrictive bars (operating in the L-T mode), was developed describing both temporal and spatial deformations (the model was also verified

with measurements). Through the modeling and measurement of 9 ME transducers with different dimensions, several effects were studied: 1) Effect of DC bias magnetic field (H_{DC}) and loading (R_L) on ME resonance frequency (f_n) and optimal operation frequency; 2) Effect of ME transducer dimension and H_{DC} on the ME quality factor; 3) Effect of H_{DC} , operation frequency, dimension, and R_L on the received power of the ME transducer. The performance of the ME transducer as a power receiver was also compared to that of an optimal coil with comparable size and frequency. By the optimal choice of the ME transducer dimension, H_{DC} , f_n , and R_L , the received power by a small ME transducer can be much higher than that of a coil; especially in applications that the size and frequency of the receiver need to be reduced.

REFERENCES

- K. Finkenzeller, RFID-Handbook, 2nd ed. Hoboken, NJ, USA: Wiley, 2003.
- [2] C. Kim, D. Seo, J. You, J. Park, and B. Cho, "Design of a contactless battery charger for cellular phone," *IEEE Trans. Ind. Electron.*, vol. 48, no. 6, pp. 1238–1247, Dec. 2001.
- [3] K. Hatanaka *et al.*, "Power transmission of a desk with a cord-free power supply," *IEEE Trans. Magn.*, vol. 38, no. 5, pp. 3329–3331, Sep. 2002.
- [4] M. Yin, D. Borton, J. Aceros, W. Patterson, and A. Nurmikko, "A 100-channel hermetically sealed implantable device for chronic wireless neurosensing applications," *IEEE Trans. Biomed. Circuits Syst.*,vol. 7, no. 2, pp. 115–128, Apr. 2013.
- [5] D. Zhou and E. Greenbaum, *Implantable Neural Prostheses 1*. New York, NY, US: Springer, 2009.
- [6] K. Chen, Z. Yang, L. Hoang, J. Weiland, M. Humayun, and W. Liu, "An integrated 256-channel epiretinal prosthesis," *IEEE J. Solid State Circuits*, vol. 45, no. 9, pp. 1946–1956, Sep. 2010.
- [7] S. Lee, H. Lee, M. Kiani, U. Jow, and M. Ghovanloo, "An inductively-powered scalable 32-channel wireless neural recording system-on-a-chip for neuroscience applications," *IEEE Trans. Biomed. Circuits Syst.*, vol. 4, no. 6, pp. 360–371, Dec. 2010.
- [8] U. Jow and M. Ghovanloo, "Design and optimization of printed spiral coils for efficient transcutaneous inductive power transmission," *IEEE Trans. Biomed. Circuits Syst.*, vol. 1, no. 3, pp. 193–202, Sep. 2007.
- [9] M. Kiani, U. Jow, and M. Ghovanloo, "Design and optimization of a 3coil inductive link for efficient wireless power transmission," *IEEE Trans. Biomed. Circuits Syst.*, vol. 5, no. 6, pp. 579–591, Dec. 2011.
- [10] M. Baker and R. Sarpeshkar, "Feedback analysis and design of RF power links for low-power bionic systems," *IEEE Trans. Biomed. Circuits Syst.*, vol. 1, no. 1, pp. 28–38, Mar. 2007.
- [11] G. McConnell, H. Rees, A. Levey, C. Gutekunst, R. Gross, and R. Bellamkonda, "Implanted neural electrodes cause chronic, local inflammation that is correlated with local neurodegeneration," *J. Neural Eng.*, vol. 6, Oct. 2009, Art. no. 056003.
- [12] J. Ho et al., "Wireless power transfer to deep-tissue microimplants," in Proc. Nat. Acad. Sci. USA, vol. 111, pp. 7974–7979, Jun. 2014.
- [13] M. Zargham and P. Gulak, "Maximum achievable efficiency in near-field coupled power-transfer systems," *IEEE Trans. Biomed. Circuits Syst.*, vol. 6, no. 3, pp. 228–245, Jun. 2012.
- [14] D. Ahn and M. Ghovanloo, "Optimal design of wireless power transmission links for millimeter-sized biomedical implants," *IEEE Trans. Biomed. Circuits Syst.*, vol. 10, no. 1, pp. 125–137, Feb. 2016.
- [15] M. Mark, T. Bjorninen, L. Ukkonen, L. Sydanheimo, and J. Rabaey, "SAR reduction and link optimization for mm-size remotely powered wireless implants using segmented loop antennas," *Biomed. Wireless Techn. Netw.* Sens. Syst., pp. 7–10, Jan. 2011.
- [16] R. Muller et al., "A minimally invasive 64-channel wireless μECoG implant," IEEE J. Solid State Circuits, vol. 50, no. 1, pp. 344–359, Jan. 2015.
- [17] A. Ibrahim and M. Kiani, "A figure-of-merit for design and optimization of inductive power transmission links for millimeter-sized biomedical implants," *IEEE Trans. Biomed. Circuits Syst.*, vol. 10, no. 6, pp. 1100–1111, Dec. 2016
- [18] J. Young, M. Wang, and I. Brezovich, "Frequency/depth-penetration considerations in hyperthermia by magnetically induced currents," *Electron. Lett.*, vol. 16, no. 10, pp. 358–359, May 1980.

- [19] IEEE standard for safety levels with respect to human exposure to electric, magnetic, and electromagnetic fields, 0 Hz to 300 GHz, IEEE Standard C95.1-2019, pp. 1–312, Oct. 2019.
- [20] R. Erfani, F. Marefat, A. Sodagar, and P. Mohseni, "Modeling and experimental validation of a capacitive link for wireless power transfer to biomedical implants," *IEEE Trans. Circuits Syst. II*, vol. 65, no. 7, pp. 923–927, Jul. 2018.
- [21] D. Seo *et al.*, "Wireless recording in the peripheral nervous system with ultrasonic neural dust," *Neuron*, vol. 91, pp. 529–539, Aug. 2016.
- [22] J. Charthad, M. Weber, T. Chang, and A. Arbabian, "A mm-sized implantable medical device (IMD) with ultrasonic power transfer and a hybrid bi-directional data link," *IEEE J. Solid State Circuits*, vol. 50, no. 8, pp. 1–13, Aug. 2015.
- [23] S. Song, A. Kim, and B. Ziaie, "Omni-directional ultrasonic powering for millimeter-scale implantable devices," *IEEE Trans. Biomed. Eng.*, vol. 62, no. 11, pp. 2717–2723, Nov. 2015.
- [24] M. Meng and M. Kiani, "Design and optimization of ultrasonic wireless power transmission links for millimeter-sized biomedical implants," *IEEE Trans. Biomed. Circuits Syst.*, vol. 11, no. 1, pp. 98–107, Feb. 2017.
- [25] A. Ibrahim, M. Meng, and M. Kiani, "A comprehensive comparative study on inductive and ultrasonic wireless power transmission to biomedical implants," *IEEE Sensors J.*, vol. 18, no. 9, pp. 3813–3826, May 2018.
- [26] S. Zuo et al., "Ultrasensitive magnetoelectric sensing system for pico-tesla magnetomyography," *IEEE Trans. Biomed. Circuits Syst.*, vol. 14, no. 5, pp. 971–984, Oct. 2020.
- [27] H. Palneedi et al., "Enhanced self-biased magnetoelectric coupling in laser annealed Pb(Zr,Ti)O₃ thick film deposited on Ni foil," ACS Appl. Mater. Interfaces, vol. 10, pp. 11018–11025, Jan. 2018.
- [28] V. Annapureddy et al., "Exceeding milli-watt powering magneto-mechano-electric generator for standalone-powered electronics," Energy Environ. Sci., vol. 11, pp. 818–829, Apr. 2018.
- [29] R. Sriramdas et al., "Large power amplification in magneto-mechanoelectric harvesters through distributed forcing," Adv. Energy Materials, vol. 10, no. 8, Feb. 2020, Art. no. 1903689.
- [30] M. Kang et al., "Magnetic field sensing by exploiting giant non-strain-mediated magnetodielectric response in epitaxial composites," Nano Lett., vol. 18, pp. 2835–2843, Apr. 2018.
- [31] T. Nan et al., "Acoustically actuated ultra-compact NEMS magnetoelectric antennas," Nature Commun., vol. 8, Aug. 2017, Art. no. 296.
- [32] G. Rizzo, V. Loyau, R. Nocua, J. Lourme, and E. Lefeuvre, "Potentiality of magnetoelectric composites for wireless power transmission in medical implants," in *Proc.* 13th Int. Symp. Med. Inf. Commun. Tech., 2019, pp. 1–4.
- [33] T. Rupp, B. Truong, S. Williams, and S. Roundy, "Magnetoelectric transducer designs for use as wireless power receivers in wearable and implantable applications," *Materials*, vol. 12, Feb. 2019, Art. no. 512.
- [34] B. Truong, E. Andersen, C. Casados, and S. Roundy, "Magnetoelectric wireless power transfer for biomedical implants: Effects of non-uniform magnetic field, alignment and orientation," *Sensors Actuators A: Phys.*, vol. 316, Dec. 2020, Art. no. 112269.
- [35] A. Singer et al., "Magnetoelectric materials for miniature, wireless neural stimulation at therapeutic frequencies," Neuron, vol. 107, no. 4, pp. 631–643, Aug. 2020.
- [36] Z. Yu et al., "MagNI: A magnetoelectrically powered and controlled wireless neurostimulating implant," *IEEE Trans. Biomed. Circuits Syst.*, vol. 14, no. 6, pp. 1241–1252, Dec. 2020.
- [37] Z. Yu *et al.*, "Multisite bio-stimulating implants magnetoelectrically powered and individually programmed by a single transmitter," in *Proc. IEEE Custom Int. Circuits Conf.*, 2021, pp. 1–2.
- [38] M. Zaeimbashi et al., "Ultra-compact dual-band smart NEMS magnetoelectric antennas for simultaneous wireless energy harvesting and magnetic field sensing," Nature Commun., vol. 12, May 2021, Art. no. 3141.
- [39] S. Dong, J. Li, and D. Viehland, "Characterization of magnetoelectric laminate composites operated in longitudinal-transverse and transversetransverse modes," *J. Appl. Phys.*, vol. 95, pp. 2625–2630, Feb. 2004.
- [40] S. Dong, J. Li, and D. Viehland, "Longitudinal and transverse magnetoelectric voltage coefficients of magnetostrictive/piezoelectric laminate composite: Theory," *IEEE Trans. Ultrason. Ferroelect. Freq. Control*, vol. 51, no. 10, pp. 794–799, Oct. 2003.
- [41] M. Bichurin, V. Petrov, S. Averkin, and A. Filippov, "Electromechanical resonance in magnetoelectric layered structures," *Phys. Solid State*, vol. 52, pp. 2116–2122, Oct. 2010.
- [42] Y. Shi, "Modeling of nonlinear magnetoelectric coupling in layered magnetoelectric nanocomposites with surface effect," *Composite Struct.*, vol. 185, pp. 474–482, Feb. 2018.
- [43] IEEE Standard on Piezoelectricity, ANSI/IEEE Std 176-1987, 1988.

- [44] IEEE Standard on Magnetostrictive Materials: Piezomagnetic Nomenclature, IEEE Std 319-1990, 1991.
- [45] A. Erturk and D. Inman, Piezoelectric Energy Harvesting, Hoboken, NJ, USA: Wiley, 2011.
- [46] D. Inman and R. Singh, Engineering Vibration, vol. 3, Englewood Cliffs, NJ, USA: Prentice Hall, 1994.
- [47] R. Sriramdas, S. Chiplunkar, R. Cuduvally, and R. Pratap, "Performance enhancement of piezoelectric energy harvesters using multilayer and multistep beam configurations," *IEEE Sensors J.*, vol. 15, no. 6, pp. 3338–3348, Jun. 2015.
- [48] M. Vopsaroiu, J. Blackburn, and M. Cain, "A new magnetic recording read head technology based on the magneto-electric effect," J. Phys. D: App. Phys., vol. 40, Aug. 2007, Art. no. 5027.
- [49] M. Sheykholeslami, Y. Hojjat, M. Ghodsi, M. Zeighami, and K. Kakavand, "Effect of magnetic field on mechanical properties in permendur," *Mater. Sci. Eng.: A*, vol. 651, pp. 598–603, Jan. 2016.
- [50] S. Verbridge, J. Parpia, R. Reichenbach, L. Bellan, and H. Craighead, "High quality factor resonance at room temperature with nanostrings under high tensile stress," *J. Appl. Phys.*, vol. 99, Jun. 2006, Art. no. 124304.
- [51] R. Sriramdas and R. Pratap, "Scaling and performance analysis of MEMS piezoelectric energy harvesters," *J. Microelectromech. Syst.*, vol. 26, no. 3, pp. 679–690, Jun. 2017.
- [52] Y. Cheng, G. Chen, D. Xuan, G. Qian, M. Ghovanloo, and G. Wang, "Analytical modeling of small, solenoidal, and implantable coils with ferrite tube core," *IEEE Microw. Wireless Comput. Lett.*, vol. 29, no. 3, pp. 237–239, Mar. 2019.
- [53] F. Alrashdan, J. Chen, A. Singer, B. Avants, K. Yang, and J. Robinson, "Wearable wireless power systems for 'ME-BIT' magnetoelectric-powered bio implants," *J. Neural Eng.*, vol. 18, no. 4, Jul. 2021, Art. no. 45011.
- [54] Y. Zhou, S. Yang, D. Apo, D. Maurya, and S. Priya, "Tunable self-biased magnetoelectric response in homogenous laminates," *Appl. Phys. Lett.*, vol. 101, no. 23, Nov. 2012, Art. no. 232905.
- [55] E. Lage et al., "Magnetic domain control and voltage response of exchange biased magnetoelectric composites," Appl. Phys. Lett., vol. 104, no. 13, Mar. 2014, Art. no. 132405.
- [56] B. Lee, D. Ahn, and M. Ghovanloo, "Three-phase time-multiplexed planar power transmission to distributed implants," *IEEE J. Emerg. Sel. Topics Power Electron.*, vol. 4, no. 1, pp. 263–272, Mar. 2016.
- [57] A. Ibrahim, A. Farajidavar, and M. Kiani, "A 64-channel wireless implantable system-on-chip for gastric electrical-wave recording," in *Proc. IEEE Sensors Conf.*, 2016, pp. 1–3.
- [58] J. DiMarco, "Implantable cardioverter-defibrillators," New England J. Med., vol. 349, no. 19, pp. 1836–1847, 2003.



Sujay Hosur (Student Member, IEEE) received the B.E. degree from Visvesvaraya Technological University, Belgaum, India, in 2017, and the M.S. degree in 2019 from The Pennsylvania State University, University Park, PA, USA, where he is currently working toward the Ph.D. degree. During his master's, his research focused on the multimodal eyelid drive system. He joined Integrated Circuits and Systems Laboratory, The Pennsylvania State University, as a master's student in 2018, and is currently continuing with ICSL for his Ph.D. degree. His research interests

include magnetoelectric devices, integrated circuit design, implantable biomedical devices, machine learning (ML), and artificial intelligence (AI).



Rammohan Sriramdas received the B.Tech. degree in mechanical engineering from Jawaharlal Nehru Technological University, Hyderabad, India, in 2005, and the M.S. and Ph.D. degrees from the Department of Mechanical Engineering, Indian Institute of Science, Bengaluru, India, in 2017. From 2006 to 2011, he was a Scientist and an Engineer with Inertial Systems Unit, Indian Space Research Organization. He was a Postdoctoral Scholar with Virginia Tech, Blacksburg, VA, USA, and an Assistant Research Professor with The Pennsylvania State University,

University Park, PA, USA. He is currently an Assistant Professor with the Department of Mechanical Engineering, Amrita Vishwa Vidyapeetham, Coimbatore campus, India. His research interests include the design and analysis of bio-inspired robotic systems, energy harvesting, and wireless power transfer.



Sumanta Kumar Karan received the Ph.D. degree from the Materials Science Centre, Indian Institute of Technology Kharagpur, Kharagpur, India. He is currently a Postdoctoral Research Scholar with the Department of Materials Science and Engineering, The Pennsylvania State University, University Park, PA, USA. His research interests include autonomous self-healing flexible piezoelectric organic crystals, high performance magneto-piezoelectric energy harvester, biodegradable magneto-piezoelectric/triboelectric generators,

and ultrasound and/or magnetic field induced devices for wireless power/data transfer and implantable applications. During his doctoral degree, he worked on high power density and energy conversion efficient polymer-graphene based self-powered piezo/triboelectric energy harvester and explored several new efficient natural bio-piezoelectric materials in the energy harvesting community. He also worked on EMI shielding materials, and fabrication of self-charging supercapacitor devices for smart electronics applications.



Shashank Priya is currently a Professor of materials science and engineering with The Pennsylvania State University, University Park, PA, USA, and serves as an Associate Vice President of research and director of strategic initiatives. He also has an Adjunct Professor appointment with the Department of Mechanical Engineering, The Pennsylvania State University and Virginia Tech, Blacksburg, VA, USA. He has authored or coauthored more than 450 peer-reviewed high impact journal papers and book chapters and more than 60 conference proceedings covering these topics. He

has authored or coauthored ten U.S. patents and edited ten books. His research interests include multifunctional materials, energy harvesting, and bio-inspired systems. His research group is interdisciplinary, consisting of materials scientists, physicists, mechanical engineers, roboticists, and electrical engineers. This allows the group to conduct integrated research addressing several aspects at the material, component, and system level. He is the Founder and Chair of the Annual Energy Harvesting Society Meeting. He is a Member of the Honorary Chair Committee for the International Workshop on Piezoelectric Materials and Applications (IWPMA). He is a Fellow of the American Ceramic Society.



Na Liu received the bachelor's degree from Central South University, Changsha, China, in 2007, the master's degree in materials science and engineering from the Shanghai Institute of Optics and Fine Mechanics, Chinese Academy of Sciences, Beijing, China, in 2010, and the Ph.D. degree from Technische Universität Darmstadt, Germany, in 2017. She is currently a Postdoctoral Scholar with Penn State University, State College, PA, USA. Since 2020, she has been working with Penn State University, as a Postdoctoral Fellow. Her research interests include scanning probe

microscopy, fabricating thermal acoustic (TA) devices, and shape memory alloys using for energy harvesting.



Mehdi Kiani (Senior Member, IEEE) received the B.S. degree from Shiraz University, Shiraz, Iran, in 2005, the M.S. degree from the Sharif University of Technology, Tehran, Iran, in 2008, and the M.S. and Ph.D. degrees in electrical and computer engineering from the Georgia Institute of Technology, Atlanta, GA, USA, in 2012 and 2013, respectively. In August 2014, he joined the Faculty of the School of Electrical Engineering and Computer Science, The Pennsylvania State University, University Park, PA, USA, where he is currently an Associate Professor. His

research interests include the multidisciplinary areas of analog, mixed-signal and power-management integrated circuits, wireless implantable medical devices, neural interfaces, and assistive technologies. He was the recipient of the 2020 NSF CAREER Award. He is currently an Associate Editor of the IEEE TRANS-ACTIONS ON BIOMEDICAL CIRCUITS AND SYSTEMS and IEEE TRANS-ACTIONS ON BIOMEDICAL ENGINEERING. He is currently a Technical Program Committee (TPC) Member of the IEEE International Solid-State Circuits Conference (ISSCC). He also served as the TPC Member of the IEEE Custom Integrated Circuits Conference (CICC) and IEEE Sensors Conference.